Comparative Results for Positioning with Secondary Synchronization Signal versus Cell Specific Reference Signal in LTE Systems

Kimia Shamaei, Joe Khalife, and Zaher M. Kassas
University of California, Riverside

BIOGRAPHIES

Kimia Shamaei is a Ph.D. candidate at the University of California, Riverside and a member of the Autonomous Systems Perception, Intelligence, and Navigation (ASPIN) Laboratory. She received her B.S. and M.S. in Electrical Engineering from the University of Tehran. Her current research interests include analysis and modeling of signals of opportunity and software-defined radio.

Joe J. Khalife is a Ph.D. student at the University of California, Riverside and a member of the ASPIN Laboratory. He received a B.E. in Electrical Engineering and an M.S. in Computer Engineering from the Lebanese American University (LAU). From 2012 to 2015, he was a research assistant at LAU. His research interests include opportunistic navigation, autonomous vehicles, and software-defined radio.

Zaher (Zak) M. Kassas is an assistant professor at the University of California, Riverside and director of the ASPIN Laboratory. He received a B.E. in Electrical Engineering from LAU, an M.S. in Electrical and Computer Engineering from The Ohio State University, and an M.S.E. in Aerospace Engineering and a Ph.D. in Electrical and Computer Engineering from The University of Texas at Austin. From 2004 through 2010 he was a research and development engineer with the LabVIEW Control Design and Dynamical Systems Simulation Group at National Instruments Corp. His research interests include estimation, navigation, autonomous vehicles, and intelligent transportation systems.

ABSTRACT

The achievable positioning precision using two different reference signals in long-term evolution (LTE) systems, namely the secondary synchronization signal (SSS) and the cell-specific reference signal (CRS), is presented. Two receiver architectures are presented: SSS-based and CRS-based. The CRS-based receiver refines the time-of-arrival (TOA) estimate obtained from the SSS signal by estimating the channel frequency response, yielding a more precise TOA estimate. Experimental results of a ground vehicle navigating with each of the presented receivers are given showing a fivefold reduction in the positioning root-mean square error with the CRS-based receiver over the SSS-based receiver.

I. INTRODUCTION

Signals of opportunity (SOPs) are an attractive navigation source in global navigation satellite system (GNSS)-challenged environments [1, 2]. The literature on SOPs answers theoretical questions on the observability and estimability of the SOPs landscape for various *a priori* knowledge scenarios [3, 4] and prescribe receiver motion strategies for accurate receiver and SOP localization and timing estimation [5–7]. Moreover, a number of recent experimental results have demonstrated receiver localization and timing via different SOPs [8–14]. Cellular SOPs are particularly attractive due to their high carrier-to-noise ratio and the large number of base transceiver stations in GNSS-challenged environments. Navigation frameworks and receiver architectures were developed for cellular code division multiple access (CDMA), which is the transmission standard of the third generation of cellular signals. Experimental results showed meter-level accuracy for CDMA-based navigation [15].

In recent years, long-term evolution (LTE), the fourth generation cellular transmission standard, has received considerable attention [16–20]. This is due to specific desirable characteristics of LTE signals, including: (1) higher transmission bandwidth compared to previous generations of wireless standards and (2) the ubiquity of LTE networks. The literature on LTE-based navigation has demonstrated several experimental results for positioning using real LTE signals [16–18, 20]. Moreover, several software-defined receivers (SDRs) have been proposed for navigation

Preprint of the 2017 ION ITM Conference
Monterey, CA, January 30–February 2, 2017

with real and laboratory-emulated LTE signals [21–23]. Experimental results with real LTE signals showed meter-level accuracy [23]. These SDRs rely on estimating the time-of-arrival (TOA) from the first peak of of the estimated channel impulse response (CIR).

There are three possible reference sequences in a received LTE signal that can be used for navigation: (1) primary synchronization signal (PSS), (2) secondary synchronization signal (SSS), and (3) cell-specific reference signal (CRS). First, the PSS is expressible in only three different sequences, each of which represents the base station (referred to as eNodeB) sectors' ID. This presents two main drawbacks: (1) the received signal is highly affected by interference from neighboring eNodeBs with the same PSS sequences and (2) the user equipment (UE) can only simultaneously track a maximum of three eNodeBs, which is not desirable in an environment with more than three eNodeBs. Another reference sequence is the SSS, which represents the cell group identifier. Second, the SSS is expressible in only 168 different sequences; therefore, it does not have the aforementioned drawbacks of the PSS. The transmission bandwidth of the SSS is less than 1 MHz, leading to low TOA accuracy in a multipath environment. However, it can provide computationally low-cost and relatively precise pseudorange information using conventional delay-locked loops (DLLs). The third reference sequence is the CRS, which is mainly transmitted to estimate the channel between the eNodeB and the UE. Therefore, it is scattered in both frequency and time and is transmitted from all transmitting antennas. The CRS is known to provide higher accuracy in estimating the TOA due to its higher transmission bandwidth [24].

This paper's objective is to study the achievable positioning precision with SSS versus CRS signals. To this end, the architectures of an SSS-based and a CRS-based SDRs are presented. Then, an extended Kalman filter (EKF) framework for navigating with LTE signals using the presented SDRs is given. Finally, experimental analysis for a ground vehicle-mounted receiver is presented for the (1) precision of the pseudoranges obtained from each of the SDRs and (2) the accuracy of the navigation solution obtained from the EKF framework.

The remainder of this paper is organized as follows. Section II provides an overview of the LTE frame structure and reference signals and discusses the signal acquisition process. Section III discusses the architecture of the SSS-based LTE SDR. Section IV provides an architecture for a CRS-based LTE SDR. Section V presents an EKF framework for navigating using LTE signals and provides experimental results showing (1) the pseudoranges obtained from each of the proposed SDRs and (2) a ground vehicle navigating via real LTE signals using the SDRs and EKF framework proposed in this paper. Concluding remarks are given in Section VI.

II. LTE FRAME AND SIGNALS

In this section, the structure of the LTE signals is outlined. Then, two types of signals that can be exploited for navigation purposes are discussed, namely (1) synchronization signals (i.e., PSS and SSS) and (2) the CRS. Finally, a method for acquiring a coarse estimate of the TOA of the LTE signal that exploits synchronization signals is discussed.

A. LTE Frame Structure

In the LTE downlink transmission protocol, the transmitted data is encoded using orthogonal frequency division multiplexing (OFDM). In OFDM, the transmitted symbols are mapped to multiple carrier frequencies called subcarriers. Fig. 1 represents the block diagram of the OFDM encoding scheme for digital transmission. The serial data symbols are first parallelized in groups of length of N_r, where N_r represents the number of subcarriers that carry data. Then, each group is zero-padded to length N_c, and the inverse fast fourier transform (IFFT) of the result is taken. To provide a guard band in the frequency-domain, N_c is set to be greater than N_r. Finally, to protect the data from multipath effect, the last L_{CP} elements of the obtained symbols are repeated at the beginning of the data, which is called cyclic prefix (CP). The transmitted symbols at the receiver can be obtained by reverting all these steps.

The obtained OFDM signals are arranged into multiple blocks, which are called frames. In an LTE system, the structure of the frame is dependent on the transmission type, which can be frequency division duplexing (FDD) or time division duplexing (TDD). Due to the superior performance of FDD over TDD [25], most network providers use FDD for LTE transmission. Therefore, this paper considers FDD frames only, and an FDD frame will be simply denoted frame.

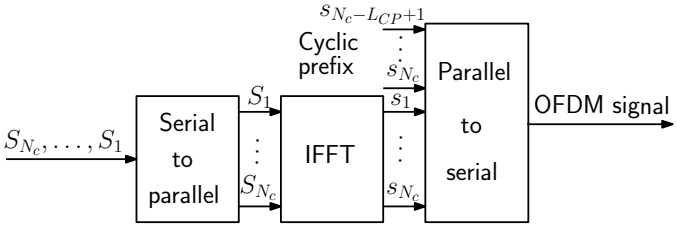

Fig. 1. OFDM transmission block diagram.

A frame is composed of 10 ms of data, which is divided into 20 slots with a duration of 0.5 ms each – equivalent to 10 subframes with a duration of 1 ms each. A slot can be decomposed into multiple resource grids (RGs), and each RG has numerous resource blocks (RBs). A RB is divided into smaller elements, namely resource elements (REs), which are the smallest building blocks of an LTE frame. The frequency and time indices of an RE are called subcarrier and symbol, respectively. The structure of the LTE frame is illustrated in Fig. 2 [26].

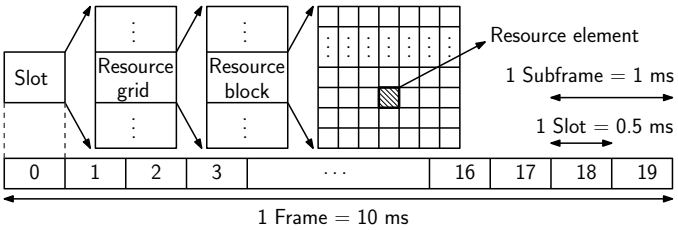

Fig. 2. LTE frame structure.

The number of subcarriers in an LTE frame, N_c, and the number of used subcarriers, N_r, are assigned by the network provider and can only take the values that are tabulated in Table I. The subcarrier spacing is typically $\Delta f = 15$ KHz. Hence, the occupied bandwidth can be calculated using $W = N_r \times \Delta f$, which is less than the assigned bandwidth shown in Table I to provide a guard band for LTE transmission.

TABLE I
LTE SYSTEM BANDWIDTHS AND NUMBER OF SUBCARRIERS.

Bandwidth (MHz)	**Total number of subcarriers**	**Number of subcarriers used**
1.4	128	72
3	256	180
5	512	300
10	1024	600
15	1536	900
20	2048	1200

When a UE receives an LTE signal, it must reconstruct the LTE frame to be able to extract the information transmitted in the signal. This is achieved by first identifying the frame start time. Then, knowing the frame timing, the receiver can remove the CPs and take the fast fourier transform (FFT) of each N_c symbols. The duration of the normal CP is 5.21 μs for the first symbol of each slot and 4.69 μs for the rest of the symbols [26]. To determine the frame timing, PSS and SSS must be acquired, which will be discussed in the next subsection.

B. Synchronization Signals

To provide the symbol timing, the PSS is transmitted on the last symbol of slot 0 and repeated on slot 10. The PSS is a length-62 Zadoff-Chu sequence which is located in 62 middle subcarriers of the bandwidth excluding the DC subcarrier. The PSS can be one of only three possible sequences, each of which maps to an integer value

$N_{ID}^{(2)} \in \{0, 1, 2\}$, representing the sector number of the eNodeB. To detect the PSS, the UE exploits the orthogonality of the Zadoff-Chu sequences and correlates the received signal with all the possible choices of the PSS, as given by

$$\begin{aligned} \text{Corr}(\boldsymbol{r}, \boldsymbol{s}_{PSS})_m &= \sum_{n=0}^{N-1} \boldsymbol{r}(n) \boldsymbol{s}_{PSS}^*(n+m)_N \\ &= \boldsymbol{r}(m) \circledast_N \boldsymbol{s}_{PSS}^*(-m)_N, \end{aligned} \tag{1}$$

where $\boldsymbol{r}(n)$ is the received signal, $\boldsymbol{s}_{PSS}(n)$ is the receiver-generated time-domain PSS sequence, N is the frame length, $(\cdot)^*$ is the complex-conjugate operator, $(\cdot)_N$ is the circular shift operator, and $\circledast_N$ is the circular convolution operator. By taking the FFT then IFFT of (1), the correlation can be rewritten as

$$\text{Corr}(\boldsymbol{r}, \boldsymbol{s}_{PSS})_m = \mathsf{IFFT}\{\boldsymbol{R}(k) \boldsymbol{S}_{PSS}^*(k)\}, \tag{2}$$

where $\boldsymbol{R}(k) \triangleq \mathsf{FFT}\{\boldsymbol{r}(n)\}$, and $\boldsymbol{S}_{PSS}(k) \triangleq \mathsf{FFT}\{\boldsymbol{s}_{PSS}(n)\}$.

The SSS is an orthogonal length-62 sequence, which is transmitted in either slot 0 or 10, in the symbol preceding the PSS, and on the same subcarriers as the PSS. The SSS is obtained by concatenating two maximal-length sequences scrambled by a third orthogonal sequence generated based on $N_{ID}^{(2)}$. There are 168 possible sequences for the SSS that are mapped to an integer number $N_{ID}^{(1)} \in \{0, \ldots, 167\}$, called the cell group identifier. The FFT-based correlation in (2) is also exploited to detect the SSS signal. Fig. 3 shows the PSS and SSS correlation results with real LTE signals.

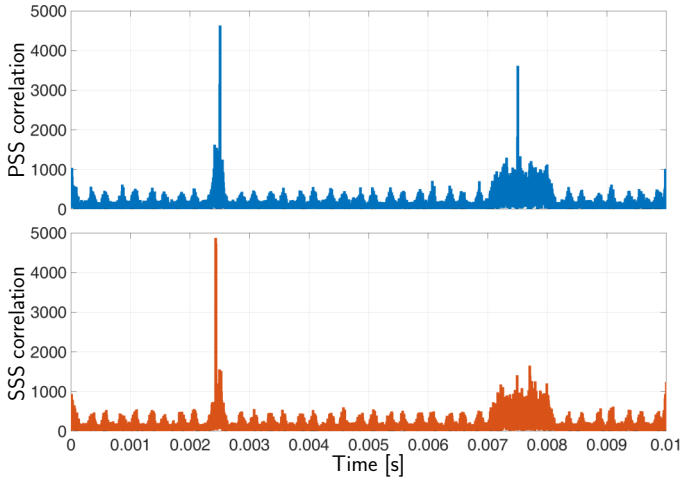

Fig. 3. PSS and SSS correlation results with real LTE signals.

Once the PSS and SSS are detected, the UE can estimate the frame start time, $\hat{t}_s$, and the eNodeB's cell ID using

$$N_{ID}^{cell} = 3N_{ID}^{(1)} + N_{ID}^{(2)}.$$

C. CRS

The CRS is a pseudo-random sequence, which is uniquely defined by the eNodeB's cell ID. It is spread across the entire bandwidth and is transmitted mainly to estimate the channel frequency response. The CRS subcarrier allocation depends on the cell ID, and it is designed to keep the interference with CRSs from other eNodeBs to a minimum. The transmitted OFDM symbol containing the CRS at the k-th subcarrier, $\boldsymbol{Y}(k)$, can be expressed as

$$\boldsymbol{Y}(k) = \begin{cases} \boldsymbol{S}(k), & \text{if } k \in A_{CRS}, \\ \boldsymbol{D}(k), & \text{otherwise}, \end{cases} \tag{3}$$

where $\boldsymbol{S}(k)$ is the eNodeB's CRS sequence, $\boldsymbol{D}(k)$ is other data signals, A_{CRS} is the set of subcarriers carrying CRS signal.

III. SSS-BASED RECEIVER

In Section II, acquiring a coarse estimate of frame timing using the PSS and SSS signals was discussed. After acquisition, the UE tracks the frame timing to estimate the TOA. The SSS is one possible sequence that a UE can exploit to track the frame timing [23]. In this section, the structure of this SSS-based tracking algorithm is discussed. Fig. 4 represents the block diagram of an SSS-based tracking loop [23]. This structure is composed of a frequency-locked loop (FLL)-assisted phase-locked loop (PLL) and a carrier-aided delay-locked loop (DLL). Each component is discussed next in detail.

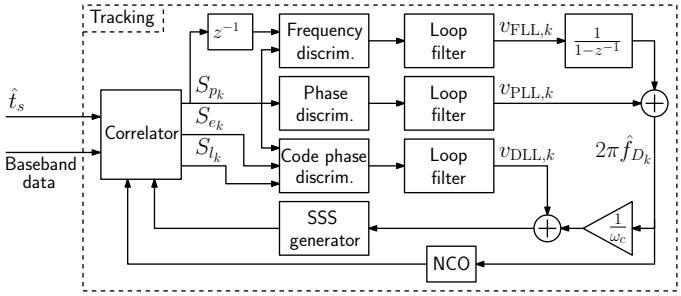

Fig. 4. SSS-based signal tracking block diagram.

A. FLL-Assisted PLL

The FLL-assisted PLL consists of a phase discriminator, a phase loop filter, a frequency discriminator, a frequency loop filter, and a numerically-controlled oscillator (NCO). Since there is no data modulated on the SSS, an `atan2` phase discriminator, which remains linear over the full input error range of $\pm\pi$, could be used without the risk of introducing phase ambiguities. A third-order PLL was used to track the carrier phase, with a loop filter transfer function given by

$$F_{\mathrm{PLL}}(s) = 2.4\omega_{n,p} + \frac{1.1\omega_{n,p}^2}{s} + \frac{\omega_{n,p}^3}{s^2}, \tag{4}$$

where $\omega_{n,p}$ is the undamped natural frequency of the phase loop, which can be related to the PLL noise-equivalent bandwidth $B_{n,\mathrm{PLL}}$ by $B_{n,\mathrm{PLL}} = 0.7845\omega_{n,p}$ [27, 28]. The output of the phase loop filter is the rate of change of the carrier phase error $2\pi\hat{f}_{D_k}$, expressed in rad/s, where $\hat{f}_{D_k}$ is the Doppler frequency. The phase loop filter transfer function in (4) is discretized and realized in state-space. The noise-equivalent bandwidth $B_{n,\mathrm{PLL}}$ is chosen to range between 4 and 8 Hz. The PLL is assisted by a second-order FLL with an `atan2` discriminator for the frequency as well. The frequency error at time step k is expressed as

$$e_{f_k} = \frac{\texttt{atan2}\left(Q_{p_k}I_{p_{k-1}} - I_{p_k}Q_{p_{k-1}}, I_{p_k}I_{p_{k-1}} + Q_{p_k}Q_{p_{k-1}}\right)}{T_{sub}},$$

where $S_{p_k} = I_{p_k} + jQ_{p_k}$ is the prompt correlation at time-step k and $T_{sub} = 0.01$ s is the subaccumulation period, which is chosen to be one frame length. The transfer function of the frequency loop filter is given by

$$F_{\mathrm{FLL}}(s) = 1.414\omega_{n,f} + \frac{\omega_{n,f}^2}{s}, \tag{5}$$

where $\omega_{n,f}$ is the undamped natural frequency of the frequency loop, which can be related to the FLL noise-equivalent bandwidth $B_{n,\mathrm{FLL}}$ by $B_{n,\mathrm{FLL}} = 0.53\omega_{n,f}$ [27]. The output of the frequency loop filter is the rate of change of the angular frequency $2\pi\hat{\dot{f}}_{D_k}$, expressed in rad/s^2. It is therefore integrated and added to the output of the phase loop filter. The frequency loop filter transfer function in (5) is discretized and realized in state-space. The noise-equivalent bandwidth $B_{n,\mathrm{FLL}}$ is chosen to range between 1 and 4 Hz.

B. Carrier-Aided DLL

Two types of discriminators for the DLL are considered: (1) coherent and (2) noncoherent [29]. The carrier-aided DLL employs these discriminators to compute the SSS code phase error using the prompt, early, and late correlations,

denoted by S_p, S_e, and S_l, respectively. The early and late correlations are calculated by correlating the received signal with an early and a delayed version of the prompt SSS sequence, respectively. The time shift between S_e and S_l is defined by an early-minus-late time t_{eml}, expressed in chips. The chip interval T_c for the SSS can be expressed as $T_c = \frac{1}{W_{SSS}}$, where W_{SSS} is the bandwidth of the synchronization signal. Since the SSS occupies only 62 subcarriers, W_{SSS} is calculated to be $W_{SSS} = 62 \times 15 = 930$ KHz, hence $T_c \approx 1.0752\mu$s.

The DLL loop filter is a simple gain K, with a noise-equivalent bandwidth $B_{n,\mathrm{DLL}} = \frac{K}{4} \equiv 0.5$ Hz. The output of the DLL loop filter v_{DLL} is the rate of change of the SSS code phase, expressed in s/s. Assuming low-side mixing, the code start time is updated according to

$$\hat{t}_{s_{k+1}} = \hat{t}_{s_k} - (v_{\mathrm{DLL,k}} + \hat{f}_{D_k}/f_c) \cdot T_{sub}.$$

Finally, the frame start time estimate is used to reconstruct the transmitted LTE frame.

IV. CRS-BASED RECEIVER

After obtaining the TOA using the SSS-based receiver, the UE could improve the TOA estimate using the CRS signal. For this purpose, the signal must be first converted to the frame structure. Then, the UE must estimate the channel frequency response $\hat{\boldsymbol{H}}(k)$ from

$$\begin{aligned}\hat{\boldsymbol{H}}(k) &= \boldsymbol{S}^*(k)\boldsymbol{R}(k) \\ &= \boldsymbol{H}(k)\left|\boldsymbol{S}^{(u')}(k)\right|^2 + \boldsymbol{V}(k),\end{aligned}$$

where $k \in A_{CRS}$ and $\boldsymbol{V}(k)$ is additive white Gaussian noise. Knowing that $\left|\boldsymbol{S}^{(u')}(k)\right|^2 = 1$, the estimate of the channel frequency response is simplified to

$$\hat{\boldsymbol{H}}(k) = \boldsymbol{H}(k) + \boldsymbol{V}(k). \tag{6}$$

By applying a Hamming window $\boldsymbol{w}(k)$ whose length is equal to the channel frequency response and taking a $2K$ point IFFT from (6), the channel impulse response can be expressed as

$$\hat{\boldsymbol{h}}(n) = \frac{1}{2K}\sum_{\kappa=0}^{K-1} \hat{\boldsymbol{H}}(\kappa)\boldsymbol{w}(\kappa)e^{\frac{j2\pi n\kappa}{2K}}.$$

where K is the length of the channel. The symbol timing error is the time shift at which the first peak of the channel impulse response occurs. Fig. 5 represents the block diagram of extracting the TOA from the CRS.

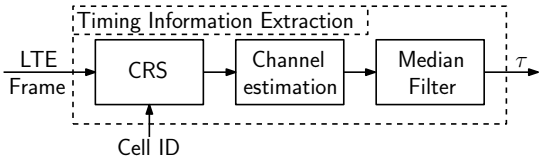

Fig. 5. Timing information extraction block diagram.

The estimated TOA obtained by the CRS is exploited as a feedback to correct the SSS-based results. Section V will demonstrate the efficacy of this feedback in multipath environments.

V. EXPERIMENTAL RESULTS

In this section, a navigation framework that employs the SDRs proposed in this paper and an EKF is described. Next, experimental results demonstrating a ground vehicle navigating using real LTE signals are presented.

A. Navigation Framework

Sections III and IV discussed how a TOA estimate can be extracted from LTE signals. By multiplying the obtained TOA estimate with the speed of light, c, a pseudorange measurement can be formed. This measurement can be

parameterized by the receiver and eNodeB states. The state of the vehicle-mounted receiver is given by

$$\boldsymbol{x}_r = \left[\boldsymbol{r}_r^{\mathsf{T}}, \dot{\boldsymbol{r}}_r^{\mathsf{T}}, c\delta t_r, c\dot{\delta} t_r\right]^{\mathsf{T}},$$

where $\boldsymbol{r}_r = [x_r, y_r, z_r]^{\mathsf{T}}$ is the receiver's three-dimensional (3-D) position vector, δt_r is the receiver's clock bias, and $\dot{\delta} t_r$ is the receiver's clock drift. The state of the i-th eNodeB is given by

$$\boldsymbol{x}_{s_i} = \left[\boldsymbol{r}_{s_i}^{\mathsf{T}}, c\delta t_{s_i}, c\dot{\delta} t_{s_i}\right]^{\mathsf{T}},$$

where $\boldsymbol{r}_{s_i} = [x_{s_i}, y_{s_i}, z_{s_i}]^{\mathsf{T}}$ is the i-th eNodeB's 3-D position vector, δt_{s_i} is the eNodeB's clock bias, and $\dot{\delta} t_{s_i}$ is the eNodeB's clock drift. The pseudorange between the receiver and i-th eNodeB can be expressed as

$$\rho_i = \|\boldsymbol{r}_r - \boldsymbol{r}_{s_i}\|_2 + c \cdot [\delta t_r - \delta t_{s_i}] + v_i,$$

where v_i is the measurement noise, which is modeled as a zero-mean Gaussian random variable with variance σ_i^2. The receiver's clock bias and drift are assumed to evolve according to the following discrete-time (DT) dynamics

$$\boldsymbol{x}_{\text{clk}_r}(n+1) = \mathbf{F}_{\text{clk}} \boldsymbol{x}_{\text{clk}_r}(n) + \boldsymbol{w}_{\text{clk}_r}(n),$$

where

$$\boldsymbol{x}_{\text{clk}_r} \triangleq \begin{bmatrix} c\delta t_r \\ c\dot{\delta} t_r \end{bmatrix}, \quad \mathbf{F}_{\text{clk}} = \begin{bmatrix} 1 & T \\ 0 & 1 \end{bmatrix}, \quad \boldsymbol{w}_{\text{clk}_r} = \begin{bmatrix} w_{\delta t_r} \\ w_{\dot{\delta} t_r} \end{bmatrix},$$

where $T \equiv T_{sub}$ is the sampling time and $\boldsymbol{w}_{\text{clk}_r}$ is the process noise, which is modeled as a DT zero-mean white sequence with covariance $\mathbf{Q}_{\text{clk}_r}$ with

$$\mathbf{Q}_{\text{clk}_r} = \begin{bmatrix} S_{\tilde{w}_{\delta t_r}} T + S_{\tilde{w}_{\dot{\delta} t_r}} \frac{T^3}{3} & S_{\tilde{w}_{\dot{\delta} t_r}} \frac{T^2}{2} \\ S_{\tilde{w}_{\dot{\delta} t_r}} \frac{T^2}{2} & S_{\tilde{w}_{\dot{\delta} t_r}} T \end{bmatrix}.$$

The terms $S_{\tilde{w}_{\delta t_r}}$ and $S_{\tilde{w}_{\dot{\delta} t_r}}$ are the clock bias and drift process noise power spectra, respectively, which can be related to the power-law coefficients, $\{h_\alpha\}_{\alpha=-2}^{2}$, which have been shown through laboratory experiments to characterize the power spectral density of the fractional frequency deviation of an oscillator from nominal frequency according to $S_{\tilde{w}_{\delta t_r}} \approx \frac{h_0}{2}$ and $S_{\tilde{w}_{\dot{\delta} t_r}} \approx 2\pi^2 h_{-2}$ [30].

The i-th eNodeBs' clock states evolve according to the same dynamic model as the receiver's clock state, except that the process noise is replaced with $\boldsymbol{w}_{\text{clk}_{s_i}} \triangleq \left[w_{\delta t_{s_i}}, w_{\dot{\delta} t_{s_i}}\right]^{\mathsf{T}}$, which is modeled as a DT zero-mean process with covariance $\mathbf{Q}_{\text{clk}_{s_i}}$ [31].

One of the main challenges in navigation with LTE signals is the unavailability of the eNodeBs' positions and clock states. It has been previously shown that the SOP position can be mapped with a high degree of accuracy whether collaboratively or non-collaboratively [31–33]. In what follows, the eNodeBs' positions are assumed to be known, and an EKF will be utilized to estimate the vehicle's position $\boldsymbol{r}_r$ and velocity $\dot{\boldsymbol{r}}_r$ states simultaneously with the difference between the receiver and each eNodeBs' clock bias and drift states. The difference between the receiver's clock state vector and the i-th eNodeB's clock state vector $\Delta\boldsymbol{x}_{\text{clk}_i} \triangleq \boldsymbol{x}_{\text{clk}_r} - \boldsymbol{x}_{\text{clk}_{s_i}}$ evolves according to

$$\Delta\boldsymbol{x}_{\text{clk}_i}(n+1) = \mathbf{F}_{\text{clk}} \Delta\boldsymbol{x}_{\text{clk}_i}(n) + \boldsymbol{w}_{\text{clk}_i}(n),$$

where $\boldsymbol{w}_{\text{clk}_i} \triangleq \left(\boldsymbol{w}_{\text{clk}_r} - \boldsymbol{w}_{\text{clk}_{s_i}}\right)$ is a DT zero-mean white sequence with covariance $\mathbf{Q}_{\text{clk}_i}$, where $\mathbf{Q}_{\text{clk}_i} \triangleq \mathbf{Q}_{\text{clk}_r} + \mathbf{Q}_{\text{clk}_{s_i}}$.

The receiver is assumed to move in a two-dimensional (2-D) plane with known height, i.e., $z(n) = z_0$ and $\dot{z}(n) = 0$, where z_0 is a known constant. Moreover, the receiver's 2-D position is assumed to evolve according to a velocity random walk, with the continuous-time (CT) dynamics given by

$$\ddot{x}_r(t) = \tilde{w}_x, \quad \ddot{y}_r(t) = \tilde{w}_y, \tag{7}$$

where $\tilde{w}_x$ and $\tilde{w}_y$ are zero-mean white noise processes with power spectral densities $\tilde{q}_x$ and $\tilde{q}_y$, respectively. The receiver's DT dynamics are hence given by

$$\boldsymbol{x}_{\text{pv}}(n+1) = \mathbf{F}_{\text{pv}}\boldsymbol{x}_{\text{pv}}(n) + \boldsymbol{w}_{\text{pv}}(n),$$

where

$$\boldsymbol{x}_{\text{pv}} \triangleq \begin{bmatrix} x_r \\ y_r \\ \dot{x}_r \\ \dot{y}_r \end{bmatrix}, \quad \mathbf{F}_{\text{pv}} = \begin{bmatrix} 1 & 0 & T & 0 \\ 0 & 1 & 0 & T \\ 0 & 0 & 1 & 0 \\ 0 & 0 & 0 & 1 \end{bmatrix},$$

and $\boldsymbol{w}_{\text{pv}}$ is a DT zero-mean white sequence with covariance $\mathbf{Q}_{\text{pv}}$, where

$$\mathbf{Q}_{\text{pv}} = \begin{bmatrix} \tilde{q}_x\frac{T^3}{3} & 0 & \tilde{q}_x\frac{T^2}{2} & 0 \\ 0 & \tilde{q}_y\frac{T^3}{3} & 0 & \tilde{q}_y\frac{T^2}{2} \\ \tilde{q}_x\frac{T^2}{2} & 0 & \tilde{q}_xT & 0 \\ 0 & \tilde{q}_y\frac{T^2}{2} & 0 & \tilde{q}_yT \end{bmatrix}.$$

The augmented state vector which will be estimated by the EKF is defined as $\boldsymbol{x} \triangleq \left[\boldsymbol{x}_{\text{pv}}^{\mathsf{T}}, \Delta\boldsymbol{x}_{\text{clk}_1}^{\mathsf{T}}, \ldots, \Delta\boldsymbol{x}_{\text{clk}_M}^{\mathsf{T}}\right]^{\mathsf{T}}$. This vector has the dynamics

$$\boldsymbol{x}(n+1) = \mathbf{F}\boldsymbol{x}(n) + \boldsymbol{w}(n),$$

where $\mathbf{F} \triangleq \text{diag}\left[\mathbf{F}_{\text{pv}}, \mathbf{F}_{\text{clk}}, \ldots, \mathbf{F}_{\text{clk}}\right]$ and $\boldsymbol{w}$ is a DT zero-mean white sequence with covariance $\mathbf{Q} \triangleq \text{diag}\left[\mathbf{Q}_{\text{pv}}, \mathbf{Q}_{\text{clk}}\right]$ and

$$\mathbf{Q}_{\text{clk}} = \begin{bmatrix} \mathbf{Q}_{\text{clk}_r} + \mathbf{Q}_{\text{clk}_{s_1}} & \mathbf{Q}_{\text{clk}_r} & \cdots & \mathbf{Q}_{\text{clk}_r} \\ \mathbf{Q}_{\text{clk}_r} & \mathbf{Q}_{\text{clk}_r} + \mathbf{Q}_{\text{clk}_{s_2}} & \cdots & \mathbf{Q}_{\text{clk}_r} \\ \vdots & \vdots & \ddots & \vdots \\ \mathbf{Q}_{\text{clk}_r} & \mathbf{Q}_{\text{clk}_r} & \cdots & \mathbf{Q}_{\text{clk}_r} + \mathbf{Q}_{\text{clk}_{s_M}} \end{bmatrix}.$$

B. Results

To evaluate the performance of the SSS- and CRS-based LTE SDRs, a field test was conducted with real LTE signals in a suburban environment. For this purpose, a mobile ground receiver was equipped with three antennas to acquire and track: (1) GPS signals and (2) LTE signals in two different bands from nearby eNodeBs. The LTE antennas were consumer-grade 800/1900 MHz cellular omnidirectional antennas and the GPS antenna was a surveyor-grade Leica antenna. The LTE signals were simultaneously down-mixed and synchronously sampled via a dual-channel universal software radio peripheral (USRP) driven by a GPS-disciplined oscillator (GPSDO). The GPS signals were collected on a separate single-channel USRP also driven by a GPSDO. It is worth mentioning that the GPSDO is only used to discipline the clock on the USRP, which is not very stable without a GPSDO. The LTE receiver was tuned to the carrier frequencies of 1955 and 2145 MHz, which are allocated to the U.S. LTE providers AT&T and T-Mobile, respectively, and the transmission bandwidth was measured to be 20 MHz. Samples of the received signals were stored for off-line post-processing. The GPS signal was processed by a Generalized Radionavigation Interfusion Device (GRID) SDR [34] and the LTE signals were processed by the proposed SSS- and CRS-based LTE SDRs. Fig. 6 shows the experimental hardware and software setup.

Over the course of the experiment, the vehicle-mounted receiver traversed a total trajectory of 2 Km while listening to 2 eNodeBs simultaneously. The position states of the eNodeBs were mapped prior to the experiment. The first part of the experiment was to evaluate the quality of the pseudoranges obtained by the SSS- and the CRS-based SDRs. To this end, the change in the pseudorange between the receiver and eNodeB 1 and 2 was calculated using the SSS- and CRS-based SDRs. The result is plotted for each eNodeB in Fig. 7 and Fig. 9, respectively. The change in true range calculated from the GPS solution is also shown in these figures. The pseudorange error obtained from the SSS-based SDR had a standard deviation of 32.72 m for eNodeB 1 and 37.49 m for eNodeB 2. The pseudorange error obtained from the CRS-based SDR had a standard deviation of 5.14 m for eNodeB 1 and 6.01 m for eNodeB

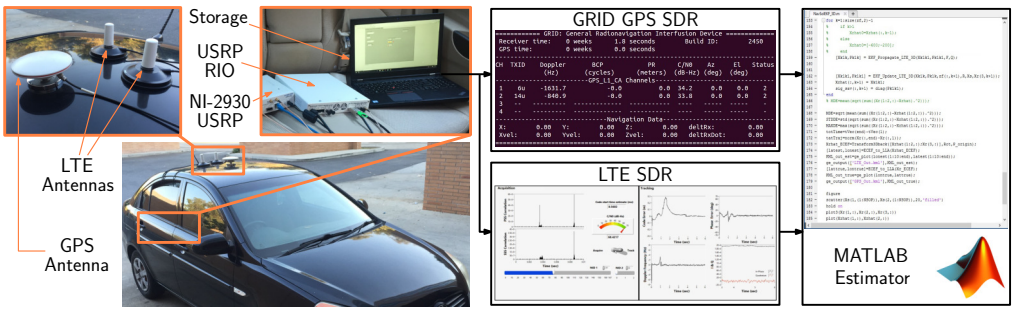

Fig. 6. Experimental setup. The LTE antennas were connected to a dual-channel National Instrument (NI) USRP RIO and the GPS antenna was connected to an NI-2930 USRP. The USRPs were driven by two independent GPSDOs.

2. Fig. 8 and Fig. 10 show the pseudorange error and its cumulative distribution function (CDF) obtained by the SSS- and CRS-based SDRs for eNodeB 1 and eNodeB 2, respectively.

On one hand, Fig. 7 and Fig. 9 show that the main cause of error in the pseudorange obtained by tracking the SSS signal is due to multipath. The estimated CIR at $t = 13.04$ s for eNodeB 1 and $t = 8.89$ s for eNodeB 2 (Fig. 7 and Fig. 9, respectively) show several peaks resulting from multipath. These peaks are the main source of pseudorange error at $t = 13.04$ s for eNodeB 1 and $t = 8.89$ s for eNodeB 2, which are around 330 m and 130 m, respectively. On the other hand, Fig. 7 and Fig. 9 show that the CRS-based receiver has a significantly lower pseudorange error compared to the SSS-based receiver in multipath environments.

It is worth mentioning that in some environments with severe multipath, the line-of-sight (LOS) signal may have a significantly lower amplitude compared to the multipath signals. In this case, the CIR peak-detection threshold must be dynamically tuned in the receiver in order to detect the LOS peak. The pseudoranges shown in Fig. 7 and Fig. 9 are obtained by tuning the receiver threshold in post-processing. Fig. 11(a) shows the pseudorange obtained without dynamically adjusting the peak-detection threshold and Fig. 11(b) depicts the in-phase and quadrature components of the prompt correlation during tracking. An instance of having a LOS peak that is significantly lower than multipath peaks is shown in the estimated CIR at $t = 40.5$ s in Fig. 9. It can be seen from this estimated CIR that the LOS peak is at approximately -40 m, whereas the highest peak of the estimated CIR, which corresponds to a multipath signal, is at approximately 400 m. Consequently, an error of approximately 440 m due to multipath will be introduced into the pseudorange, as shown in 11(a). Moreover, Fig. 11(b) shows that the receiver loses track of the signal at $t = 40.5$ s.

The second part of the experiment was to navigate using LTE signals exclusively and via the EKF framework discussed in the previous subsection. For this purpose, the receiver's position and velocity along with the difference of clock biases between the receiver and each eNodeB as well as the difference of clock drifts were estimated dynamically. To make the problem observable, it is assumed that the receiver had access to GPS before navigating with LTE signals; hence, the receiver had full knowledge of its initial state [4].

The environment layout as well as the true and estimated receiver trajectories are shown in Fig. 12. The root mean squared error (RMSE) between the GPS and SSS-based navigation solutions along the traversed trajectory was calculated to be 50.46 m with a standard deviation of 41.07 m and a maximum error of 419.66 m. The RMSE between the GPS and CRS-based navigation solutions was calculated to be 9.32 m with a standard deviation of 4.36 m and a maximum error of 33.47 m. Theses results are summarized in Table II.

TABLE II

Experimental results [in meters] comparing navigation solutions obtained from SSS-based and CRS-based SDRs.

LTE Receiver	**RMSE**	**Standard deviation**	**Maximum error**
SSS	50.46	41.07	419.66
CRS	9.32	4.36	33.47

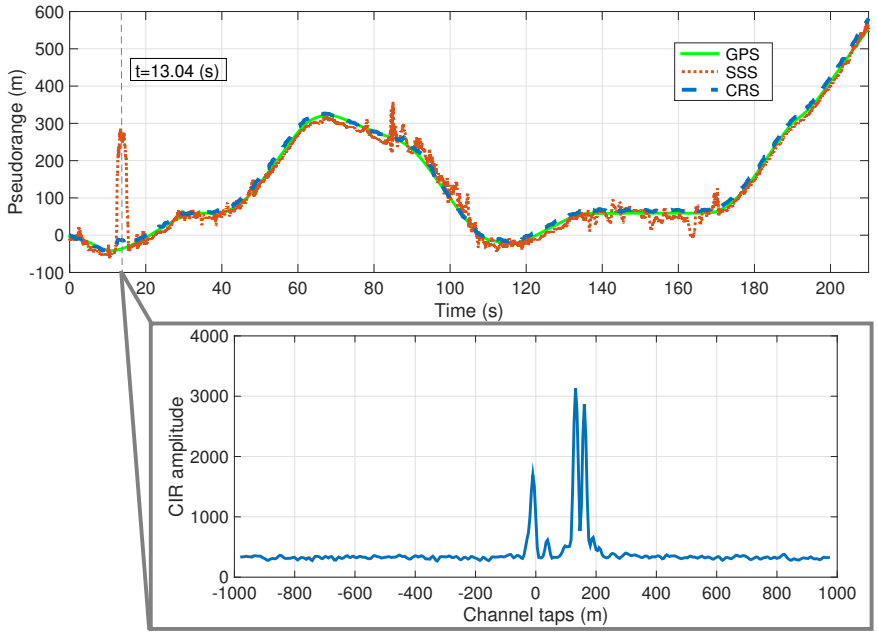

Fig. 7. Estimated change in pseudorange and estimated CIR at $t = 13.04$ s for eNodeB 1. The change in the pseudorange was calculated using: (1) SSS pseudoranges, (2) CRS pseudoranges, and (3) true ranges obtained using GPS.

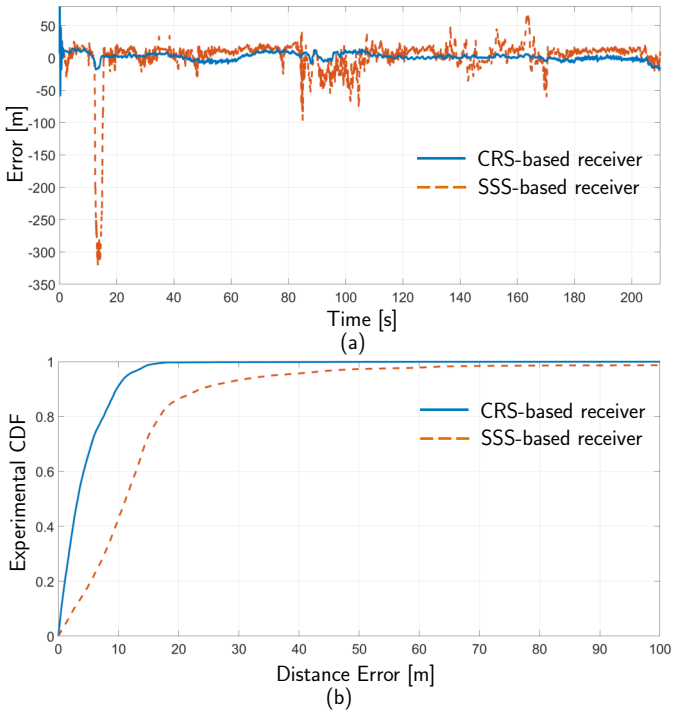

Fig. 8. (a) Error of the change in pseudorange between (1) GPS and SSS and (2) GPS and CRS. (b) CDF of the error in (a).

It is worth mentioning that there is a slight mismatch between the true vehicle's dynamical model and the assumed model in (7). The receiver was moving on a road, mostly in straight segments. The velocity random walk model used by the EKF does not take into consideration the trajectory constraints. Therefore, the EKF might allow the vehicle's position and velocity estimates to move freely. This model mismatch will cause the estimation error to become larger. In order to minimize the mismatch between the true and assumed model, multiple models for the vehicle's dynamics may be used to accommodate the different behaviors of the vehicle in different segments of the

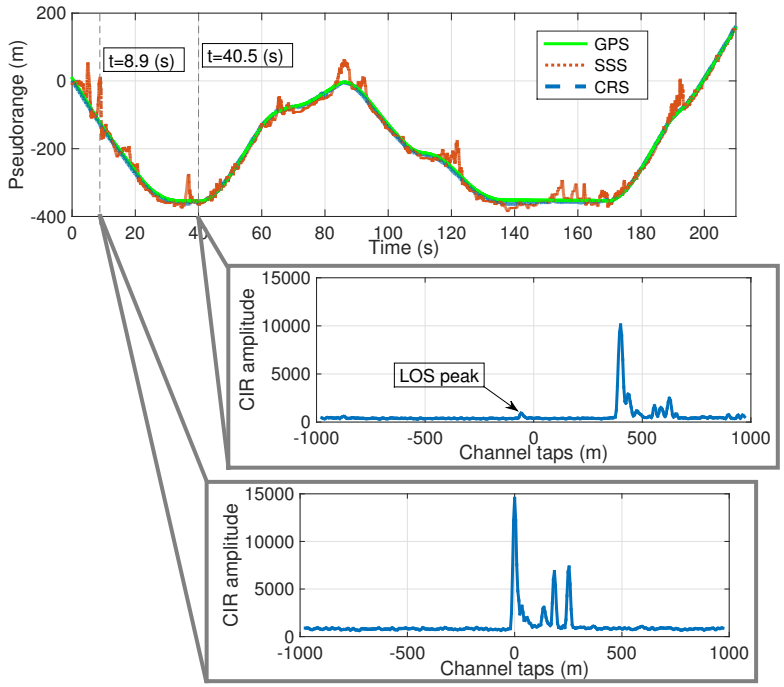

Fig. 9. Estimated change in pseudorange and estimated CIR at $t = 8.89$ s and $t = 40.5$ s for eNodeB 2. The change in the pseudorange was calculated using: (1) SSS pseudoranges, (2) CRS pseudoranges, and (3) true ranges obtained using GPS.

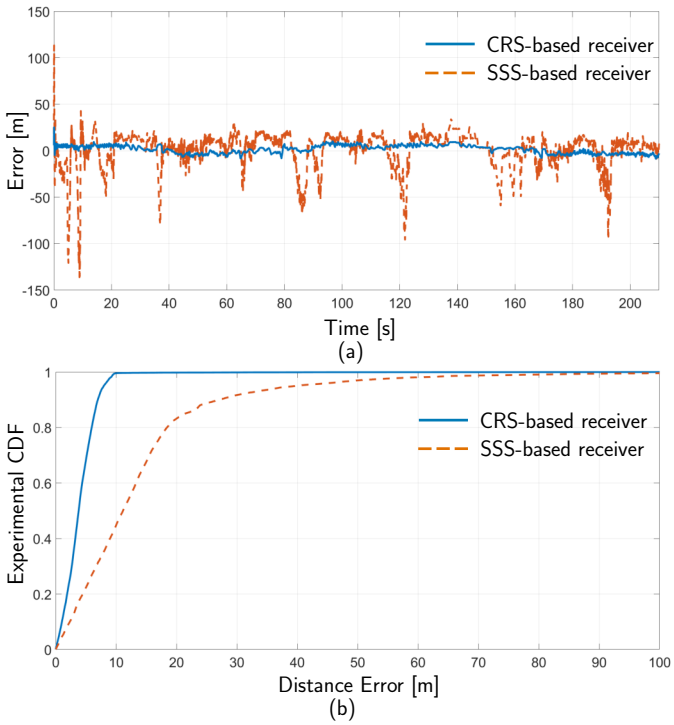

Fig. 10. (a) Error of the change in pseudorange between (1) GPS and SSS and (2) GPS and CRS. (b) CDF of the error in (a).

trajectory. Alternatively, an inertial measurement unit (IMU), which is available in many practical applications, can be used to propagate the state of the vehicle. This will also aid in alleviating multipath-induced errors [14].

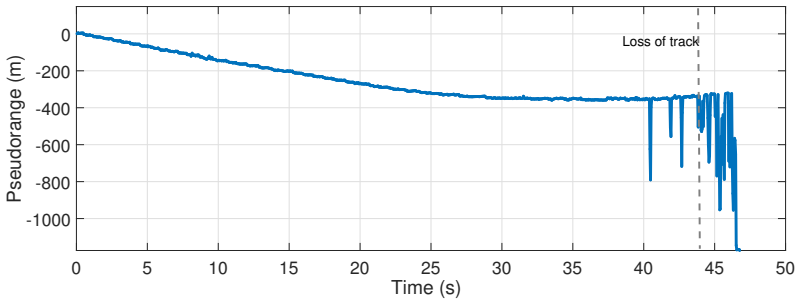

Fig. 11. Tracking results for eNodeB 2: (a) pseudorange obtained without dynamically tuning the peak-detection threshold and (b) in-phase and quadrature components of the prompt correlation during tracking. Fig. (b) shows that the receiver loses track when the threshold is not tuned to detect the LOS signal in severe multipath environments.

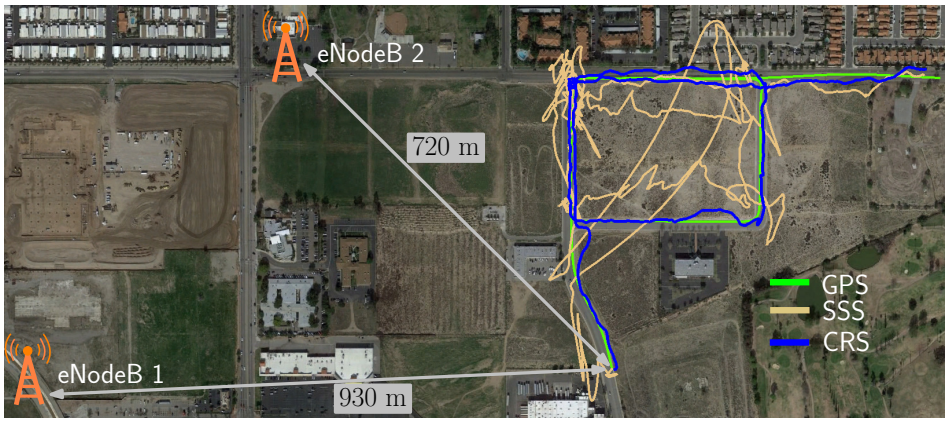

Fig. 12. Vehicle-mounted receiver's GPS trajectory and trajectories estimated with LTE SSS and CRS signals. Also shown are the LTE eNodeBs' locations.

VI. CONCLUSION

This paper presented two SDR architectures for positioning with LTE signals. The first architecture relies on tracking the SSS, which has a bandwidth of around 1 MHz. The second architecture exploits the CRS, which has a bandwidth of up to 20 MHz. In the latter, the CIR is first estimated using the CRS, and a TOA estimate is obtained by detecting the first peak of the estimated CIR. The precision of the pseudorange measurement obtained from each receiver is evaluated using real LTE signals. Experimental results showing a ground vehicle equipped with the proposed LTE SDRs navigating using real LTE signals in an EKF framework were provided. The results show an RMSE of 50.46 m for the SSS-based SDR and an RMSE of 9.32 m for the CRS-based SDR over a 2 Km trajectory.

ACKNOWLEDGMENT

This work was supported in part by the Office of Naval Research (ONR) under Grant N00014-16-1-2305.

References

[1] J. Raquet and R. Martin, "Non-GNSS radio frequency navigation," in *Proceedings of IEEE International Conference on Acoustics, Speech and Signal Processing*, March 2008, pp. 5308–5311.

[2] Z. Kassas, "Collaborative opportunistic navigation," *IEEE Aerospace and Electronic Systems Magazine*, vol. 28, no. 6, pp. 38–41, 2013.

[3] Z. Kassas and T. Humphreys, "Observability analysis of opportunistic navigation with pseudorange measurements," in *Proceedings of AIAA Guidance, Navigation, and Control Conference*, vol. 1, August 2012, pp. 1209–1220.

[4] ——, "Observability analysis of collaborative opportunistic navigation with pseudorange measurements," *IEEE Transactions on Intelligent Transportation Systems*, vol. 15, no. 1, pp. 260–273, February 2014.

[5] ——, "Motion planning for optimal information gathering in opportunistic navigation systems," in *Proceedings of AIAA Guidance, Navigation, and Control Conference*, August 2013, 551–4565.

[6] Z. Kassas, A. Arapostathis, and T. Humphreys, "Greedy motion planning for simultaneous signal landscape mapping and receiver localization," *IEEE Journal of Selected Topics in Signal Processing*, vol. 9, no. 2, pp. 247–258, March 2015.

[7] Z. Kassas and T. Humphreys, "Receding horizon trajectory optimization in opportunistic navigation environments," *IEEE Transactions on Aerospace and Electronic Systems*, vol. 51, no. 2, pp. 866–877, April 2015.

[8] M. Rabinowitz and J. Spilker, Jr., "A new positioning system using television synchronization signals," *IEEE Transactions on Broadcasting*, vol. 51, no. 1, pp. 51–61, March 2005.

[9] J. McEllroy, "Navigation using signals of opportunity in the AM transmission band," Master's thesis, Air Force Institute of Technology, Wright-Patterson Air Force Base, Ohio, USA, 2006.

[10] L. Merry, R. Faragher, and S. Schedin, "Comparison of opportunistic signals for localisation," in *Proceedings of IFAC Symposium on Intelligent Autonomous Vehicles*, September 2010, pp. 109–114.

[11] P. Thevenon, S. Damien, O. Julien, C. Macabiau, M. Bousquet, L. Ries, and S. Corazza, "Positioning using mobile TV based on the DVB-SH standard," *NAVIGATION, Journal of the Institute of Navigation*, vol. 58, no. 2, pp. 71–90, 2011.

[12] K. Pesyna, Z. Kassas, and T. Humphreys, "Constructing a continuous phase time history from TDMA signals for opportunistic navigation," in *Proceedings of IEEE/ION Position Location and Navigation Symposium*, April 2012, pp. 1209–1220.

[13] C. Yang and T. Nguyen, "Tracking and relative positioning with mixed signals of opportunity," *NAVIGATION, Journal of the Institute of Navigation*, vol. 62, no. 4, pp. 291–311, December 2015.

[14] J. Morales, P. Roysdon, and Z. Kassas, "Signals of opportunity aided inertial navigation," in *Proceedings of ION GNSS Conference*, September 2016, pp. 1492–1501.

[15] J. Khalife, K. Shamaei, and Z. Kassas, "A software-defined receiver architecture for cellular CDMA-based navigation," in *Proceedings of IEEE/ION Position, Location, and Navigation Symposium*, April 2016, pp. 816–826.

[16] F. Knutti, M. Sabathy, M. Driusso, H. Mathis, and C. Marshall, "Positioning using LTE signals," in *Proceedings of Navigation Conference in Europe*, April 2015.

[17] M. Driusso, F. Babich, F. Knutti, M. Sabathy, and C. Marshall, "Estimation and tracking of LTE signals time of arrival in a mobile multipath environment," in *Proceedings of International Symposium on Image and Signal Processing and Analysis*, September 2015, pp. 276–281.

[18] M. Ulmschneider and C. Gentner, "Multipath assisted positioning for pedestrians using LTE signals," in *Proceedings of IEEE/ION Position, Location, and Navigation Symposium*, April 2016, pp. 386–392.

[19] C. Chen and W. Wu, "3D positioning for LTE systems," *IEEE Transactions on Vehicular Technology*, vol. PP, no. 99, pp. 1–1, 2016.

[20] M. Driusso, C. Marshall, M. Sabathy, F. Knutti, H. Mathis, and F. Babich, "Vehicular position tracking using LTE signals," *IEEE Transactions on Vehicular Technology*, vol. PP, no. 99, pp. 1–1, 2016.

[21] J. del Peral-Rosado, J. Lopez-Salcedo, G. Seco-Granados, F. Zanier, P. Crosta, R. Ioannides, and M. Crisci, "Software-defined radio LTE positioning receiver towards future hybrid localization systems," in *Proceedings of International Communication Satellite Systems Conference*, October 2013, pp. 14–17.

[22] J. del Peral-Rosado, J. Parro-Jimenez, J. Lopez-Salcedo, G. Seco-Granados, P. Crosta, F. Zanier, and M. Crisci, "Comparative results analysis on positioning with real LTE signals and low-cost hardware platforms," in *Proceedings of Satellite Navigation Technologies and European Workshop on GNSS Signals and Signal Processing*, December 2014, pp. 1–8.

[23] K. Shamaei, J. Khalife, and Z. Kassas, "Performance characterization of positioning in LTE systems," in *Proceedings of ION GNSS Conference*, September 2016, pp. 2262–2270.

[24] J. del Peral-Rosado, J. Lopez-Salcedo, G. Seco-Granados, F. Zanier, and M. Crisci, "Achievable localization accuracy of the positioning reference signal of 3GPP LTE," in *Proceedings of International Conference on Localization and GNSS*, June 2012, pp. 1–6.

[25] FDD/TDD comparison. [Online]. Available: https://www.qualcomm.com/media/documents/files/fdd-tdd-comparison.pdf

[26] 3GPP, "Evolved universal terrestrial radio access (E-UTRA); physical channels and modulation," 3rd Generation Partnership Project (3GPP), TS 36.211, January 2011. [Online]. Available: http://www.3gpp.org/ftp/Specs/html-info/36211.htm

[27] E. Kaplan and C. Hegarty, *Understanding* GPS*: Principles and Applications*, 2nd ed. Artech House, 2005.

[28] W. Ward, "Performance comparisons between FLL, PLL and a novel FLL-assisted-PLL carrier tracking loop under RF interference conditions," in *Proceedings of ION GNSS Conference*, September 1998, pp. 783–795.

[29] A. van Dierendonck, P. Fenton, and T. Ford, "Theory and performance of narrow correlator spacing in a GPS receiver," *Journal of the Institute of Navigation*, vol. 39, no. 3, pp. 265–283, September 1992.

[30] A. Thompson, J. Moran, and G. Swenson, *Interferometry and Synthesis in Radio Astronomy*, 2nd ed. John Wiley & Sons, 2001.

[31] Z. Kassas, V. Ghadiok, and T. Humphreys, "Adaptive estimation of signals of opportunity," in *Proceedings of ION GNSS Conference*, September 2014, pp. 1679–1689.

[32] Z. Kassas and T. Humphreys, "The price of anarchy in active signal landscape map building," in *Proceedings of IEEE Global Conference on Signal and Information Processing*, December 2013, pp. 165–168.

[33] J. Morales and Z. Kassas, "Optimal receiver placement for collaborative mapping of signals of opportunity," in *Proceedings of ION GNSS Conference*, September 2015, pp. 2362–2368.

[34] T. Humphreys, J. Bhatti, T. Pany, B. Ledvina, and B. O'Hanlon, "Exploiting multicore technology in software-defined GNSS receivers," in *Proceedings of ION GNSS Conference*, September 2009, pp. 326–338.